Gas diffusion in water-saturated underground porous media: From micro to macro scale study

Journal of Energy Storage 173 (2026) 123049

Contents lists available at ScienceDirect

Journal of Energy Storage

journal homepage: www.elsevier.com/locate/est

Research papers

Gas diffusion in water-saturated underground porous media: From micro to macro scale study

Cristina Serazio [a], Eloisa Salina Borello [a,*], Dario Viberti [a]

[a] Department of Environment, Land and Infrastructure Engineering, Politecnico di Torino, Corso Duca degli Abruzzi 24, 10129, Turin, Italy

ARTICLE INFO

Keywords:
Underground gas storage
Bulk diffusion coefficient
Effective diffusion coefficient
Pore-scale simulation

ABSTRACT

Design and implementation of underground storage of H_2 and CO_2 require reliable and calibrated simulation models capable of predicting injected fluid behavior and its interaction with geological formation and native fluids at field scale over geological timescale. Molecular diffusion of gas through formation water in reservoir, aquifer, and caprock influences various mechanisms related to the dissolution, such as the activation of microbial activity and the trapping phenomena and, in particular, the long-term containment of the stored or sequestered gas. This project focuses on characterizing the diffusive term, which describes the molecular diffusion of dissolved gas through water-saturated porous media. Here, the bulk diffusion coefficient adopted at the microscale is rescaled to obtain the effective diffusion coefficient representing the porous medium at the macroscale through pore space morphology description based on tomographic images. Two approaches are adopted and compared: an established one involving a pore-scale numerical simulator to assess diffusion tortuosity, which is then used in a correlation to estimate the effective diffusion coefficient; an innovative workflow involving fitting the pore-scale numerical solution of the diffusion–transport equation to the analytical solution of Fick's second law for a homogeneous representative elementary volume (REV). To this end, a 1D solution of Fick's second law is derived under appropriate initial and boundary conditions. Due to the lack of nano-CT caprock data, the methodology was applied to low-porosity, tortuous rocks. The provided results should be regarded as conservative estimates; the methodology must be reapplied to nano-CT images of actual caprocks for field-scale predictions.

1. Introduction

The shift towards green and renewable energy involves underground gas storage, either of CO_2 or H_2 [1]. Long-term CO_2 underground storage is regarded as an essential mitigation option to reduce greenhouse gases in the atmosphere and mitigate climate change [2]. CCUS (Carbon Capture, Utilization, and Storage) encompasses all the methods and technologies to remove CO_2 from industrial flue gas and from the atmosphere, followed by CO_2 recycling or safe and permanent storage options [3]. On the other hand, Underground Hydrogen Storage (UHS) [4] is a technology under evaluation as a potential solution to compensate for the natural fluctuations in the production of electricity from natural resources, such as wind or solar radiation, which depend on the availability of the specific energy source. Hydrogen obtained by the conversion of electrical energy into fuel gas, Power-to-Gas (P2G) [5], can be stored for later use when required.

Underground storage of CO_2 or H_2 can benefit from the knowledge gained from natural gas storage practices. In gas reservoirs, evidence proves the sealing capacity of reservoir caprocks to prevent upward gas migration: CH_4 diffusion through caprocks is negligible even over geological times. However, there are notable differences between H_2, CO_2 and CH_4, both in terms of physical properties (such as viscosity and molecular size) and chemical characteristics (such as chemical reactivity). As a result, diffusion of H_2 and CO_2 through reservoir caprocks has to be properly evaluated.

Caprocks are made of fine grains such as clay particles, and/or they have been subjected to specific diagenetic processes such as dissolution/recrystallization [6]. They are characterized by a moderate bulk porosity composed of an intricate network of micropores (<2 nm) and mesopores (2–50 nm) and poor interconnection [7]. This tortuous pathway significantly hinders fluid flow, and it is quantified by a high hydraulic tortuosity factor between 2 and 10 [7]. Small pores imply a high entry capillary pressure. Moreover, the intricate porous morphology results in a low permeability [8], reduced by six orders of magnitude or more,

* Corresponding author.
E-mail address: eloisa.salinaborello@polito.it (E. Salina Borello).

https://doi.org/10.1016/j.est.2026.123049
Received 30 July 2025; Received in revised form 31 March 2026; Accepted 4 June 2026
Available online 14 June 2026

compared to the permeability in the reservoir zone [6]. Despite the very low permeability, diffusion coefficients can be reduced by only one or two orders of magnitude compared to bulk values [6].

In caprocks, pores are saturated with brine. The gas first dissolves in the water and then diffuses through it [6,9–12]. Solubility and bulk diffusion coefficient (D_b) of CH_4, H_2, and CO_2 in pure water are shown in Table 1.

At the pore scale (microscale), gas molecules diffuse within the saturated interconnected pore space according to the bulk diffusivity of the gas in the brine. At the continuum scale (macroscale), however, the presence of the solid matrix modifies the accessible pathways and effectively slows down diffusion with respect to the diffusivity that would occur in an equivalent bulk volume of brine. Pore network morphology, primarily its porosity and tortuosity, controls how strongly the medium impedes diffusive transport [19]. This leads to an effective diffusion coefficient (macroscale diffusion), which is lower than the bulk value (microscale diffusion). Thermodynamic conditions of the geological formation used for underground storage could have a significant impact on the bulk diffusion coefficient, and in turn on the effective diffusion. An increase in temperature enhances molecular mobility and decreases viscosity, leading to higher diffusion coefficients. Compared to temperature, pressure has a weaker influence because brine is slightly compressible. However, if we consider a fixed temperature, the increase in brine viscosity at reservoir pressure compared to ambient pressure corresponds to a decrease in diffusivity. This behavior can be expressed by the standard empirical correlation for estimating the diffusivity of a dilute dissolved gas in a liquid [20,21]:

$$D_b = 1.1728 \times 10^{-16} \frac{T\sqrt{\chi_l M_l}}{\mu_l V_g^{0.6}} \tag{1}$$

where D_b is in m^2/s, V_g is the solute (gas in our case) molar volume at the normal boiling point in m^3/kmol, T is the temperature in K, μ_l is the solvent viscosity (brine in our case) in Pa s, χ_l is the solvent association parameter and M_l is the solvent molecular weight.

Recently, some efforts have been devoted to the experimental assessment of the gas diffusion into typical sealing lithotypes for both H_2, e.g. [22–29], and CO2, e.g. [6,30–34]. The obtained values are summarized in Table 2.

In this work, we present an innovative workflow for characterizing the effective diffusion coefficient of gas in saturated porous media at the macroscale (i.e. under the continuum hypothesis), based on rescaling the bulk diffusion that occurs at the microscale within the pore space. The methodology is based on pore-scale numerical simulations of the diffusion equation performed on a simulation domain based on 3D tomographic images. Solving the diffusion equation within the pore geometry yields the spatial and temporal evolution of dissolved-gas concentration. By averaging the resulting 3D solution over a significant number of cross sections, a time-dependent concentration profile on an equivalent homogeneous 1D REV is obtained. The effective diffusion coefficient is then calculated by fitting an analytical 1D solution of Fick's second law - derived under appropriate initial and boundary conditions - to the resulting time-dependent concentration profile.

The obtained effective diffusivity values were compared with the ones calculated by the established workflow applying a literature empirical correlation, where diffusion tortuosity was estimated from the pore-scale CFD simulation.

OpenFOAM v11 numerical simulator [35] was adopted for pore-scale simulation on grids replicating binarized micro-CT scan images of rocks; known bulk diffusivity of gas in brine was imposed within the porous domain.

As literature nano-CT data of caprock are not available, three real rock geometry images from the literature were considered: the 3D binarized images of the well-characterized Berea sandstone, a low-permeability sandstone (Parker, 10 mD), and a salt sample with very low porosity (0.08%). Since caprock pore structures are typically more tortuous, less porous, and dominated by nanometric pores, the resulting diffusivity values should be regarded as conservative.

Nevertheless, the aim of this work is to provide a methodological workflow to estimate effective diffusivity using a tomographic image. The methodology bridges pore-scale models, based on well-characterized bulk gas diffusion in water, and reservoir-scale models, which rely on effective diffusion, governed by the medium's pore structure. Such a parameter is critical for simulations of Underground Storage of H_2 and CO_2, particularly for predicting gas migration through the caprock over time.

Given that experimental estimation of effective diffusion coefficient is complex and expensive, the presented methodology enables improved Underground Fluid Storage reservoir characterization using available data. Moreover, unlike the established workflow, it does not rely on empirical correlations, reducing methodological bias and enhancing physical consistency.

Table 1
Solubility and bulk diffusion coefficient in pure water [13–18].

Gas	Solubility in water (g/kg)		Bulk diffusion coefficient ($\times 10^{-9}$ m^2/s)	
	@ 20 °C, 1 atm	@ 50 °C, 120 bar	@ 20 °C, 1 atm	@ 50 °C, 120 bar
CH_4	0.023	1.28	1.62	0.039
H_2	0.0016	0.18	4.58	0.0808
CO_2	0.16	9.9	1.67	0.0365

2. Materials and methods

The methodology relies on pore-scale numerical simulations of the diffusion equation carried out on a computational domain derived from 3D tomographic images. In the present work, the tomographic images were already binarized (Section 2.1). In general, binarization is required to separate high-resolution 3D micro-CT scans into two distinct phases: solid grains and void space (pores). To this end, thresholding based on the bimodal histogram of image intensities can be employed [36]. A detailed discussion of binarization techniques is beyond the scope of this paper.

The workflow is summarized in Fig. 1. Given the bulk diffusion coefficient D_b, expressing the diffusion of gas in brine within the pore space, the diffusion equation is numerically solved (Section 2.2) on the binarized 3D porous domain. The time and space evolution of the dissolved gas concentration, $C(x, y, z, t)$, diffusing from the inlet source to the outlet through the water-saturated porous medium, along the x-direction, is determined.

By averaging the resulting 3D solution over a significant number of cross sections (on the y-z plane), a concentration profile $C(x, t)$ on an equivalent homogeneous 1D REV is obtained (see Section 2.3 for details).

Fitting an analytical 1D solution of Fick's second law, derived in Appendix A, to the resulting concentration profile $C(x, t)$ at fixed timesteps (t_n), the fitted $D_e(t_n)$ values are obtained (see Section 2.3 for details). This matching value varies over time due to the geometry of the pore spaces and converges to an asymptotic value as the concentration approaches 1 in the entire domain. The effective diffusion coefficient D_e is then estimated as the asymptotic value of the fitting. The criteria applied to select the t_n corresponding to asymptotic D_e was formalized as

$$I(t_n) \geq 0.95 \quad \wedge \quad err_{rel}(t_n) \leq 10^{-3} \tag{2}$$

where

$$I(t_n) = \frac{1}{L}\int_0^L C(x, t_n)dx \tag{3}$$

is the integral mean of the profile, that satisfies $\lim_{n\to\infty} I(t_n) = 1$, and

Table 2
Diffusivity of H_2 and CO_2 in sealing lithotypes.

		Formation	Depth	Porosity	Dry/wet	Pressure & temperature	Values
H_2	[29]	Boom clay	200–300 m	36–43%	Saturated	T: 25°C P: up to 5 bar	4.2×10^{-12} m^2/s to 1.6×10^{-10} m^2/s -
	[26]	Boom clay	200–300 m	31–45%	Saturated	T: 25°C P: ambient	3.0×10^{-11} m^2/s
	[22]	Boom clay	200–300 m	31–45%	Saturated	T: 25°C	5×10^{-12} m^2/s to 4×10^{-10} m^2/s
	[24]	Callovo-Oxfordian clay	430–550 m	–	Dry	T: 90 and 120 °C P: 0.45 bar	1.4×10^{-7} m^2/s
	[23]	Callovo-Oxfordian clay	430–550 m	–	Wet	–	1.1×10^{-11} m^2/s
	[25]	Boom clay	200–300 m	–	Saturated	T: ambient (21 °C) P: 10 bar	2.64×10^{-10} m^2/s
	[28]			33.2%	Dry and wet	T: ambient P: 0.2–0.8 atm	1×10^{-10} m^2/s to 6×10^{-8} m^2/s
	[27]	Caprock samples (late Neogene)	–	28–35%	Saturated	T: 20°–22 °C P: 40 bar	8×10^{-11} m^2/s (fresh) 1.1×10^{-8} m^2/s (long stored) 1.8×10^{-10} m^2/s (re-saturated)
CO_2	[6]	Dogger formation		6%		T: 30 and 23 °C	2.4×10^{-10} m^2/s and 1.5×10^{-10} m^2/s
	[30]	Muderong Shale	1454 mbsf	20%	Saturated	T: 50 °C P: 6 MPa	3.0×10^{-11}–4.81×10^{-11}
	[31]	Pelitic rocks			Saturated		10^{-9} to 10^{-11} m^2/s
	[33]	Munsterland Basin	128 and 813 m	15% and 6%	Saturated t	T: 28 °C P: 5 MPa	7.8×10^{-11} to 1.2×10^{-10} m^2/s

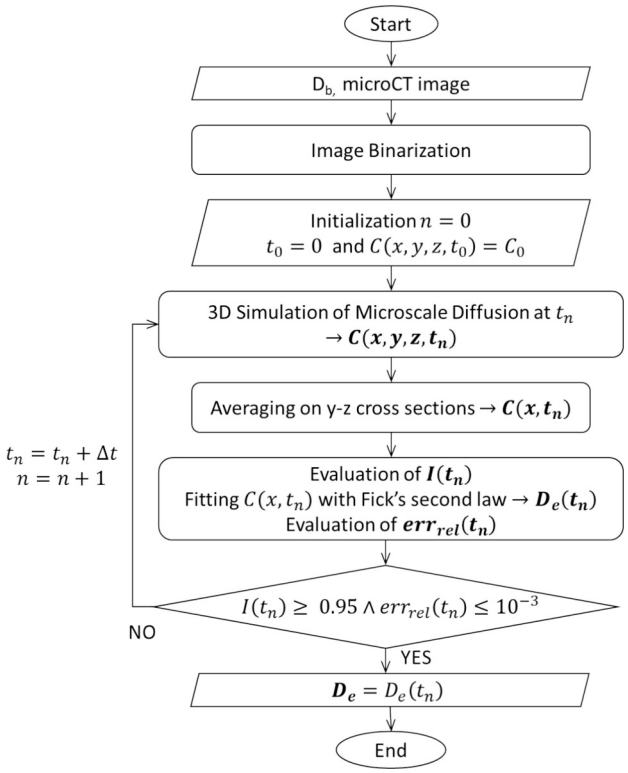

Fig. 1. Workflow for estimating the macroscale effective gas diffusion coefficient (D_e) in saturated porous media, obtained by rescaling the microscale bulk diffusion coefficient (D_b) within the pore space. C is the gas concentration, diffused from the inlet source to the outlet through the water-saturated porous medium, along the x-direction. Variables shown in boldface correspond to the outputs generated at each stage of the workflow.

$$err_{rel}(t_n) = \frac{|D_e(t_n) - D_e(t_{n-1})|}{|D_e(t_n)|} \quad (4)$$

quantifies the relative discrepancy of the fitted values computed at two successive timesteps. Such a criterion ensures that the domain was extensively explored by the diffusion simulation (i.e., $I(t)$ close to 1), while the rate of variation between two consecutive steps can be considered small.

For comparison purposes, a well-established literature empirical correlation for effective diffusivity estimation is presented in Section 2.4. The correlation relies on bulk diffusion, tortuosity and porosity; diffusion tortuosity, estimated from pore-scale CFD simulations presented in Section 2.2, was adopted for the calculation.

2.1. Samples

Since caprock pores are typically nanometric, micro-CT imaging cannot resolve their structure. Nano-computed tomography (nano-CT) is a high-resolution imaging technique representing an advancement over micro-CT technology [37]; however, nano-CT data for caprock remain scarce in the literature.

Rock computed tomography (CT) images were collected from the Digital Rock Portal and the Imperial College Consortium on Pore-scale Imaging and Modelling database. Among the micro-CT images available, three rock geometries were selected (Fig. 2), characterized by low porosity and appreciable tortuosity: Berea sandstone [38,39], Synthetic Rock Salt [40], and Parker sandstone [41,42]. Available details provided in the literature are summarized in Table 3. The selected samples are characterized by micrometric pores, porosity and permeability values greater than those of a typical shale caprock, which is characterized by porosities in the range 0.1–14% [43], permeability in the range 9×10^{-6}–6×10^{-3} mD [43], pore-throat size in the range 1–500 nm with a distribution mode around 8–20 nm [44–46] and tortuosity in the range of 2–10 [7]. Since the pore structure of a caprock is generally more tortuous, less porous, and characterized by nanometric pores (i.e., constrictivity factor <1), diffusivity values estimated for the sand samples represent a cautionary estimation. Nevertheless, the presented work is meant to provide a methodological workflow for the microscale to macroscale diffusivity assessment, starting from a tomographic image.

2.2. Microscale diffusion simulation

In the current project, pore-scale diffusion simulations were performed using the Finite Volume simulator OpenFOAM v11 [35]. The simulation domains consisted of unstructured regular hexahedral grids replicating the binarized micro-CT scans shown in Fig. 2. They were generated by exploiting the *snappyHexMesh* utility constrained to the triangulated surface of the sample grains. No mesh refinement was applied. The key parameters of the grid are summarized in Table 4.

The "pluggable" solver *scalarTransport* was then employed. This post-

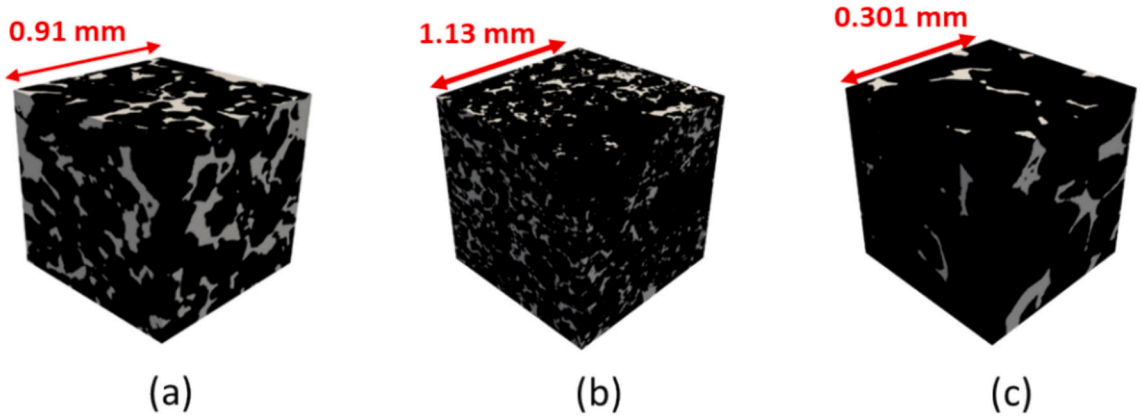

Fig. 2. Binarized micro-CT samples of (a) Berea sandstone, (b) Parker sandstone, and (c) Salt.

Table 3
Considered rock samples.

Sample	Type	Sample size (mm)	Resolution (μm/px)	ϕ (–)	k (mD)
Berea	Sandstone	0.914 × 0.914 × 0.914	5.345	0.2	1286
Parker	Sandstone	1.1273 × 1.1273 × 1.1273	7.002	0.12	10
Salt	Salt	0.301 × 0.301 × 0.301	1.881	0.08	Not available

Table 4
Simulation grid parameters.

Sample	Cell length (μm)	Grid size (# cells)
Berea	5.3	10^6
Parker	3.5	$3.7\ 10^6$
Salt	1.9	$3.5\ 10^5$

processing module evolves a passive scalar diffusion-transport equation within the investigated domain, taking as input the bulk molecular diffusive coefficient (D_b), a source term (S_C) and the velocity field ($\boldsymbol{u}$), calculated by solving the Navier-Stokes equations:

$$\frac{\partial C}{\partial t} + \nabla\cdot(\boldsymbol{u}C) - \nabla\cdot(D_b\nabla C) = S_C \tag{5}$$

In the current implementation, the dissolved gas concentration variable $C(x,y,z,t)$ was supposed to be dimensionless and normalized. Since the focus was on isolating the pure diffusion phenomenon, the velocity field was set equal to zero, as was the source term.

We assumed that the pores were initially saturated with pure water at standard conditions, implying a zero concentration of solute (gas) in the whole domain as the initial condition of the simulation. The evolution in time and space was driven by the Dirichlet boundary condition imposed at the inlet, i.e. $C(x=0,t)=1$, while the impervious condition was imposed on the throat walls and the outlet surface by requiring that $\nabla C\cdot\hat{\boldsymbol{n}}=0$, where $\hat{\boldsymbol{n}}$ is the unit normal vector to the boundary surfaces.

The gas in water bulk diffusion coefficient (D_b) was set equal to 10^{-9} m^2/s, which is representative of the order of magnitude available in literature, as shown in Table 1.

Simulations were carried out until the solute concentration approached the value of 1 throughout the whole 3D domain (Fig. 3a and b).

2.3. Macroscale diffusion coefficient from analytical solution of Fick's second law

Gas diffusion in water-saturated rocks at the macroscale, parametrized through the effective diffusion coefficient (D_e), corresponds to the diffusion of the gas within a homogeneous REV with a behavior equivalent to the microscopic porous media. As a consequence, the D_e value

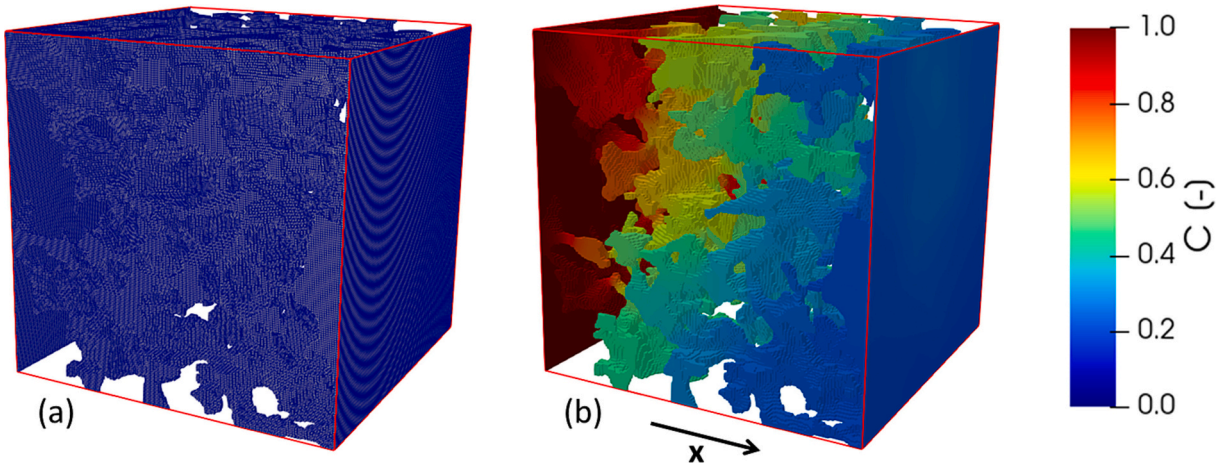

Fig. 3. (a) Simulation grid; (b) concentration evolution in time.

can be estimated by approximating the concentration distribution obtained by microscale simulation of a porous domain (Section 2.2) with the analytical solution on an equivalent macroscale homogeneous REV. In the simulated cases, the homogeneous REV is a 1D finite domain [0, L] with a constant concentration ($C_0 = 1$) imposed at the inlet boundary and a zero-gradient at the outlet. The diffusion problem is formalized as:

$$\frac{\partial C}{\partial t} = D_e \frac{\partial^2 C}{\partial x^2} \tag{6}$$

$$C = 0 \quad x > 0 \quad t = 0$$

$$C = 1 \quad x = 0 \quad t > 0$$

$$\frac{\partial C}{\partial x} = 0 \quad x = \mathrm{L} \quad t > 0$$

The equation is also known as Fick's second law [47]. The corresponding analytical solution reads (see Appendix A for details):

$$C(x,t) = 1 - \frac{2}{L}\sum_{i=1}^{+\infty} \frac{\sin(\lambda_n x)}{\lambda_n} e^{-\lambda_n^2 D_e t} \tag{7}$$

where $\lambda_n = \frac{(2n-1)\pi}{2L} \quad \forall n > 0$.

The best fitting effective diffusion D_e was then assessed by applying the least squares method to the profiles reconstructed from the simulated concentration maps (see Section 2.2) and the analytical solution (Eq. (7)).

The evolution of the concentration profile along the x-direction over time was then assessed by:

1. Slicing the computational domain with a series of equispaced planes orthogonal to the main diffusion direction (x-axis) (Fig. 4a)
2. Averaging the concentration cell values over each slice and assigning the resulting value to the x-coordinate of the slice's centroid (Fig. 4b)

$$C(slice) = \frac{\int_{slice} C\, dA}{A_s} \tag{8}$$

where A_s is the area of the slice.

This resulting curve represents the distribution of the solute (gas) concentration in water along the main diffusion direction for each timestep of the simulation. It can be approximated with the solution of the diffusion equation in a one-dimensional finite domain at different times, obtained using an effective diffusion coefficient that accounts for both D_b and the structure of the pores. In other words, it represents the link between the description of the diffusion phenomenon at the scale of the pores (where bulk diffusion coefficient is adopted) and the phenomenon at the scale of the whole sample (where the effective diffusion coefficient is adopted).

2.4. Macroscale diffusion coefficient from empirical correlations

Gas diffusion in brine saturated porous rocks at the macroscale, called effective diffusivity (D_e), is primarily influenced by the microscale diffusion of gas through the fluid filling the pores (D_b), as well as by the structure of the pores, in terms of tortuosity ($\tau > 1$), the effective porosity (ϕ) and a dimensionless factor called constrictivity ($\delta \in (0,1]$) [19,48–52]:

$$D_e = D_b \frac{\phi}{\tau^2} \delta \tag{9}$$

Constrictivity factor represents the hindrance to which the fluid is subject when travelling to pores of varying cross section (A_{yz}) [19,53]:

$$\delta = \frac{\sqrt{max\, A_{yz} \times min\, A_{yz}}}{mean\, A_{yz}} \tag{10}$$

Other authors associate the constrictivity with the reduction of the effective diffusion due to an increase in viscosity, compared to the bulk viscosity of the solvent, caused by the proximity of the pore wall [54]. A relationship explicitly accounting for Knudsen diffusion is given by [51]:

$$\delta = \frac{D_K}{D_b + D_K} \tag{11}$$

where D_K is the Knudsen diffusion, i.e., the diffusion that occurs when a molecule diffuses within a space that has dimensions comparable to or smaller than the mean free path of the molecule itself [51]:

$$D_K = \frac{d_{pore}}{3}\sqrt{\frac{8RT}{\pi M}} \tag{12}$$

For liquid-filled pores, the constrictivity value can be related to the ratio of the kinetic diameter of the diffusing molecules (d_m) to the mean pore size (d_{pore}) [55]:

$$\delta = exp\left(-4.6\frac{d_m}{d_{pore}}\right) \tag{13}$$

According to Eqs. (11) and (13), constrictivity is only important if the size of the solute becomes comparable to the size of the pore. For the considered gases, the solute size is reported in Table 5, and the trend of δ

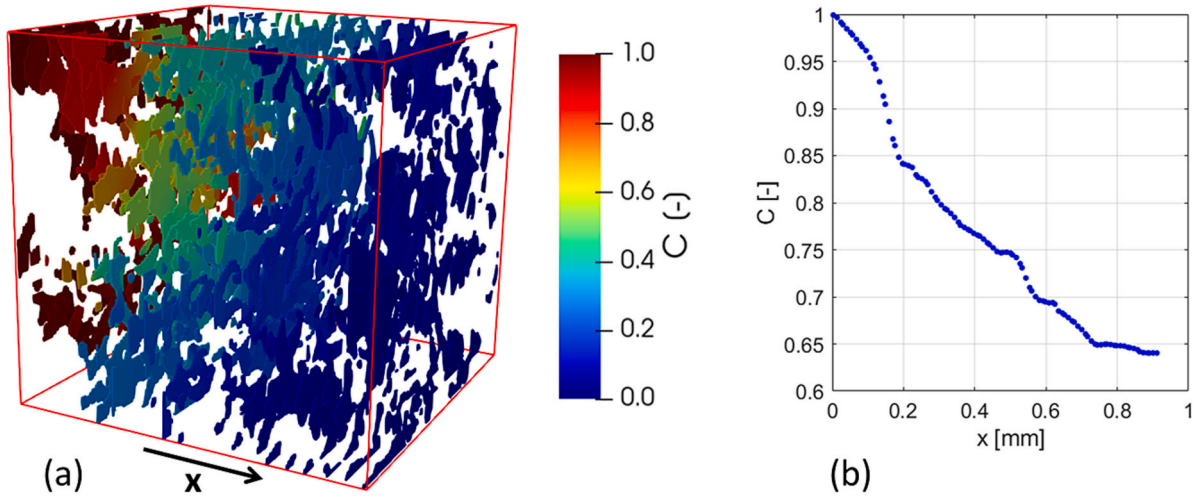

Fig. 4. Reconstruction of the Concentration profile from simulated field (Fig. 3): (a) slicing of the domain; (b) representation of the average value along the x-direction.

Table 5
Kinetic diameter of water and gas molecules for storage [57].

Molecule	Kinetic diameter (nm)
H_2O	0.265
CO_2	0.330
CH_4	0.380
H_2	0.289

vs. d_{pore} (Eq. (13)) is shown in Fig. 5. As a consequence, in the considered scenarios we can assume δ=1. In caprocks, the constrictivity may further reduce effective diffusion. The application of an algorithm for pore diameter determination from 3D image, as the one presented in [56], can be applied to the binarized nano-CT image to determine the representative pore diameter (d_{pore}) and, in turn, estimate the corresponding constrictivity (δ), using Eq. (13). However, such a reduction is not expected to be severe. By way of example, in caprock samples analyzed by [44–46] the modal pore diameter of caprocks falls within the 8–50 nm range, corresponding to $\delta \approx 0.8 - 0.97$.

Tortuosity accounts for the complexity of the pore structure morphology. It can be defined as the ratio between the effective length of the flow path to the straight-line distance in the macroscopic flow direction. Different definitions are reported in the literature, according to the considered transport process (hydraulic, electrical, diffusional, and thermal), along with a geometrical definition [49,58]. In previous work, we estimated the hydraulic and geometric tortuosity of the samples [56,59–62].

Here we focus on the diffusion tortuosity (τ_D), that we estimate by numerical simulation at the pore scale (Section 2.2). According to the definition provided by [63]:

$$\tau_D = \frac{\sum_{cells}|\boldsymbol{J}|}{\sum_{cells}J_x} \tag{14}$$

where $\boldsymbol{J}$ is the vector diffusive flux, defined as

$$\boldsymbol{J} = -D_b \nabla C \tag{15}$$

and J_x is the component along the main diffusion direction, i.e. the direction orthogonal to the imposed inlet source.

3. Results and discussion

To estimate a representative effective diffusion coefficient (D_e) for the three selected samples, the workflow introduced in the previous sections (Fig. 1) was applied.

The distribution in the pore space of the dissolved gas concentration and the corresponding average profiles are shown in the following sequence of images (Figs. 6, 7, and 8), where we selected five timesteps, named t_1 to t_5, such that $I(t)$ (Eq. (3)) approached fixed values (i.e., 0, 0.1, 0.25, 0.5, 0.75). In Figs. 6b, 7b, and 8b the simulated concentration profile averaged on y-z sections (blue) is compared with the 1D analytical solution evaluated using both the fitted coefficient ($D_e(t_n)$) at the corresponding timestep t_n (red) and the asymptotic coefficient (D_e) (green).

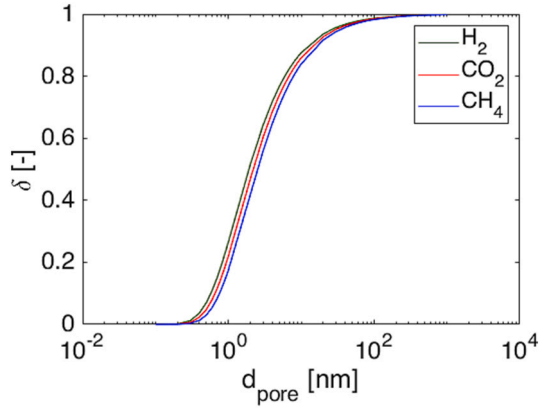

Fig. 5. Constrictivity vs. pore dimension (Eq. (13)).

The relative error ($err_{rel}(t_n)$, Eq. (4)) obtained when convergence criterion is met is equal to 6.48 10^{-5}, 3.41 10^{-4}, and 9.29 10^{-4} for the Berea, Parker and Salt scenarios, respectively. Fitting error analysis vs. simulation time is reported on Fig. 9. Since the three samples differ in size, porosity, and tortuosity, diffusion phenomenon would evolve over different time scales in the three domains.

A sensitivity to the imposed tolerance criterion (Eq. (2)) was performed. To this end, a different asymptotic value was calculated as $D_e(t_n) : I(t_n) = 0.9$. Choosing a D_e not completely stabilized ($I(t_n) = 0.9$) produce a poor coefficient of determination R^2 especially in the late time of the phenomenon (Fig. 10); this behavior is particularly evident in the Parker (Fig. 10b) and Salt (Fig. 10c) cases. However, when most of the domain was already explored by diffusion simulation, the obtained diffusivity value is not very sensitive to the adopted criterion parameters. In fact, the relative discrepancy between D_e calculated at $t_n : I(t_n) = 0.90$ and at $t_n : I(t_n) = 0.95$ is 0.21%, 4.2% 3.3% for the Berea, Parker and Salt scenarios, respectively.

In Berea scenario, good correspondence is observed between the simulated concentration profile, averaged on y-z cross sections, and the analytical concentration profile obtained with the fitting diffusion coefficient ($D_e(t_n)$) at all the considered timesteps (Fig. 6). The agreement is attributed to an internal structure that does not exhibit significant heterogeneities (Fig. 11). Conversely, in the other scenarios the simulated concentration profile is not as convex as the analytical one (Figs. 7 and 8). These irregularities are attributed to the connectivity of the pores of the samples. In the central region of Parker, porosity and pore connectivity are markedly reduced (Fig. 12): many porous pathways are interrupted or deviated to the presence of a compact grain region. This pronounced heterogeneity in the pore distribution is responsible for the observed significant deviation from the analytical concentration profile, which models the behavior of a homogeneous equivalent medium. Recalling that each value of the reconstructed profile corresponds to the average concentration over a given slice, it is clear that slices with a reduced local porosity (i.e. a reduced number of pore cells) act as bottlenecks, causing an accumulation of solute and slowing down the propagation of further into the domain. This is clearly visible in Fig. 12, where there is a correspondence between a decreasing trend of the local porosity (i.e. the measure of the porosity for each slice <0.1) and dissolved gas accumulation in the "upstream" points. Similar behavior is observed for Salt scenario, although discrepancies from analytical profile are less pronounced (Figs. 8 and 13).

The simulated evolution of concentration in both time and space also allowed for the assessment of the sample's diffusion tortuosity (τ_D, Eq. (14)). Similarly to D_e, the tortuosity value changes in time and approaches its asymptotic value when the solute concentration becomes homogenously distributed throughout the entire domain. The trend of τ_D for all three samples is shown at the top of Fig. 14.

The assessed diffusive tortuosity values were compared (Table 6) with the geometric tortuosity (τ_g), estimated using an A*-based path-finding algorithm, and with the hydraulic tortuosity (τ_h), derived from the stationary velocity field obtained through incompressible single-phase CFD simulations with OpenFOAM v11. Interested readers can refer to Panini et al. [59] for details. The three types of tortuosity (geometric, hydraulic, and diffusive) are consistent. Differences in the values are due to their different transport processes [58,64]. Hydraulic tortuosity defines the tortuous path of fluid flow (advection) driven by pressure gradients. It reflects both pore constrictions and the requirement that fluid particles remain on streamlines instead of taking shortcuts. For this reason, the hydraulic path length is greater than the

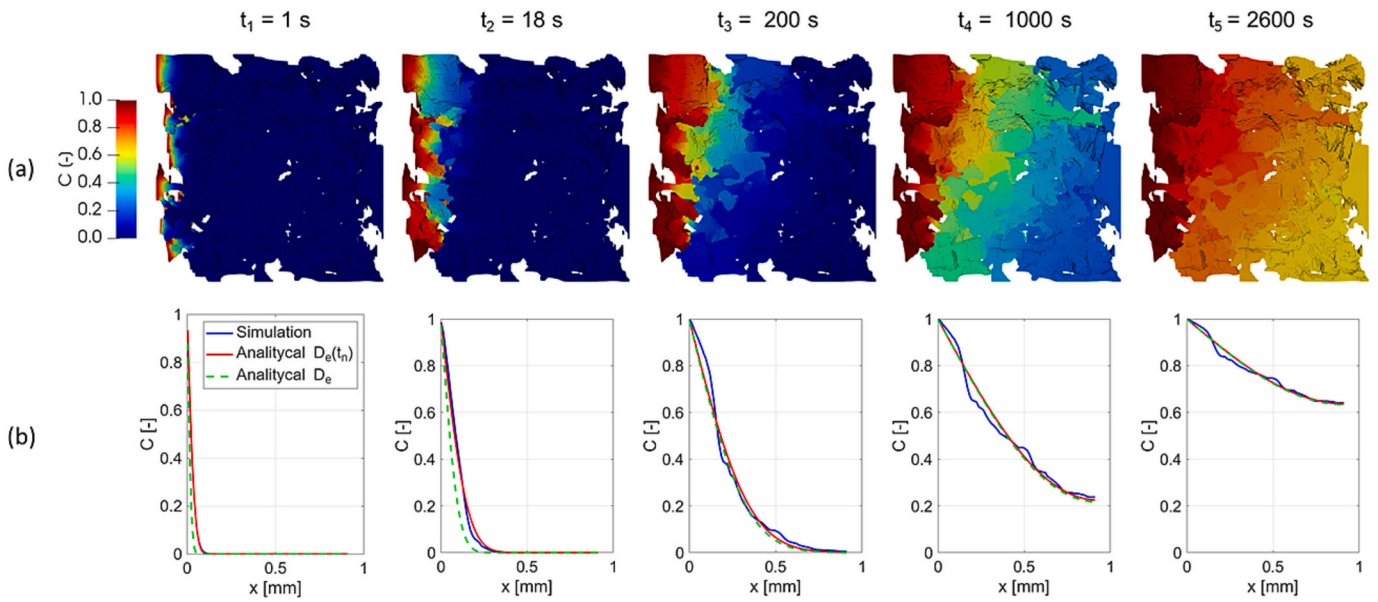

Fig. 6. Berea scenario: (a) Simulated concentration distribution at different simulation times and (b) corresponding numerical estimate of effective diffusivity by fitting analytical solution (Eq. (7)) at different timesteps.

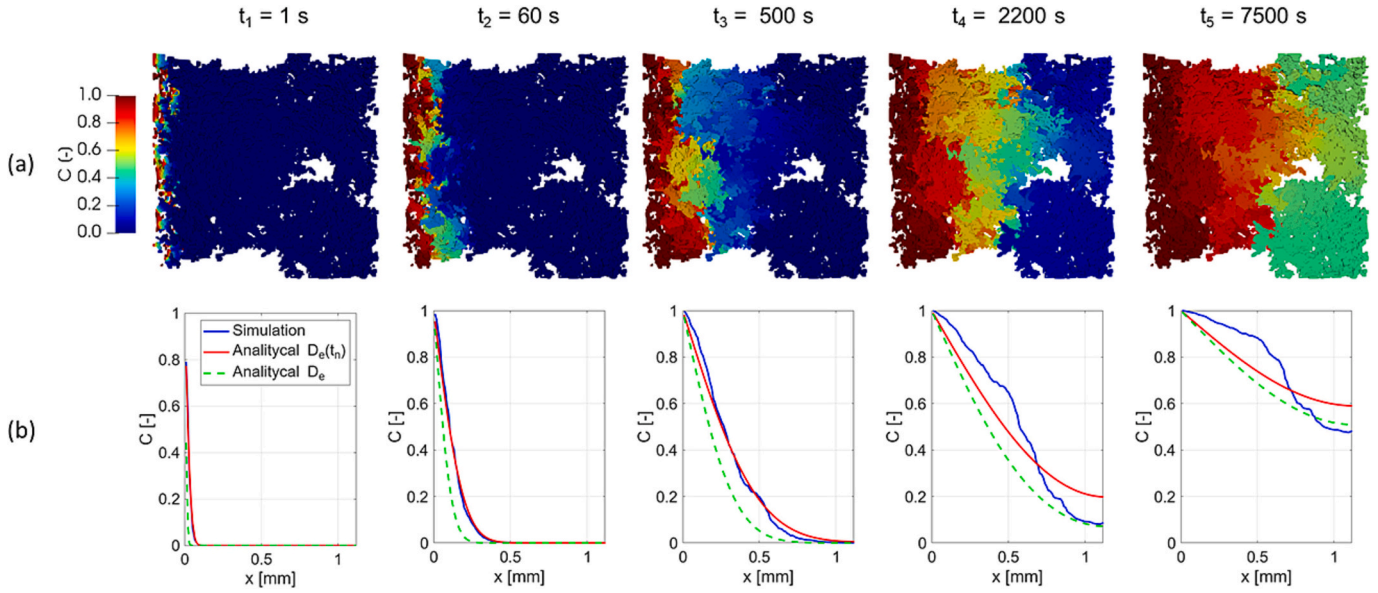

Fig. 7. Parker scenario: (a) Simulated concentration distribution at different simulation times and (b) corresponding numerical estimate of effective diffusivity by fitting analytical solution (Eq. (7)) at different timesteps.

geometric path length. On the other hand, the effective flow paths through connected pores are dominated by larger pores and fractures, thus being generally less convoluted than diffusivity ones. Diffusion tortuosity describes the path of molecules moving by random motion (Brownian motion), which tends to cover all the connected pores, not only the shortest paths or the most effective paths for the flow. A similar behavior was observed by [65] in synthetic porous media, with increasing impact for decreasing porosity.

The effective diffusion coefficients obtained with the proposed workflow, i.e. the asymptotic values of the fitted Fick's law, were compared (Table 6) with those calculated through correlation (Eq. (9)), where the numerically estimated τ_D values were adopted. Results showed good consistency, nevertheless the proposed workflow proved to be more cautionary, being higher for a factor 2 for Berea scenario to 3.5 for Salt scenario. Underestimation in the correlation estimate arises from the limited representation of the pore structure. In fact, the correlation approach (Eq. (9)) relies on porosity (accounting for pore volume), tortuosity (accounting for pore interconnection), and constrictivity (accounting for Knudsen diffusion). However, such parameters cannot capture other relevant aspects of pore space morphology such as pore size distribution (micropores vs. macropores), pore shape (rounded, elongated, or slit-shaped) and presence of bottlenecks. Conversely, being based on binarized tomographic image, the proposed workflow integrates all the morphological aspects of pore geometry, thus being more physically consistent. Results were also comparable with experimental values from literature on saturated sealing lithotypes (Table 2).

The obtained effective diffusivity values are strongly affected by sample pore structure, which is responsible for the reduction of the diffusivity from the bulk value of a factor 0.166 for Berea, 0.0737 for

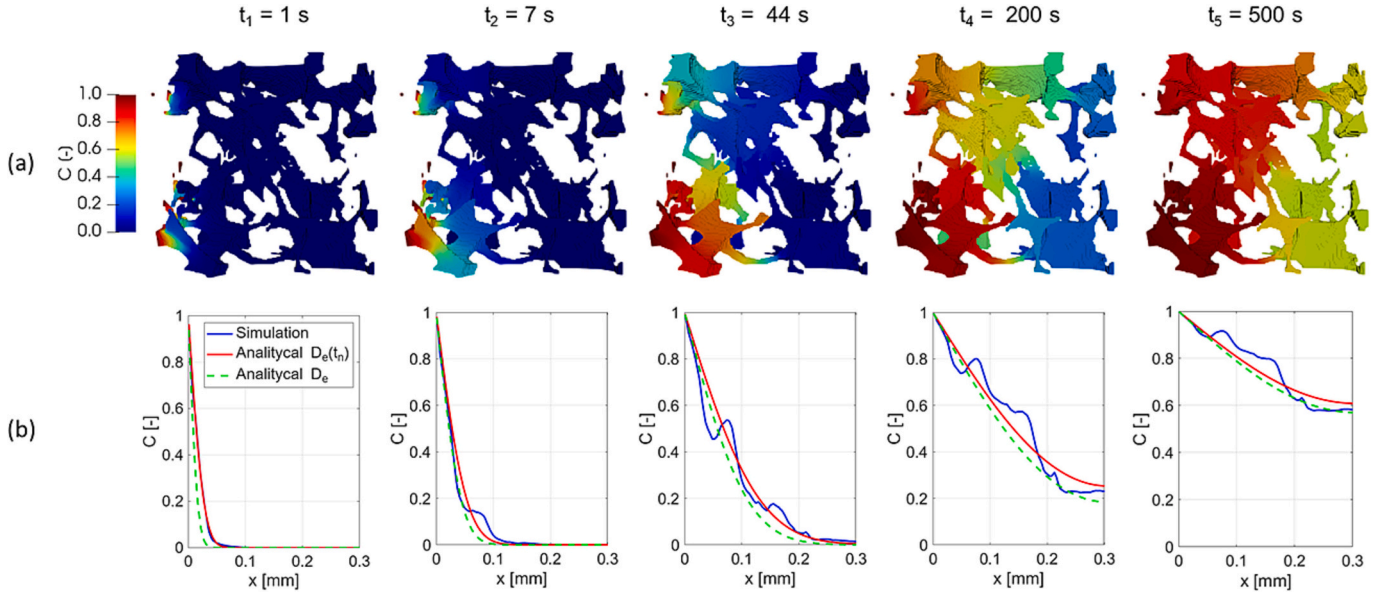

Fig. 8. Salt scenario: (a) Simulated concentration distribution at different simulation times and (b) corresponding numerical estimate of effective diffusivity by fitting analytical solution (Eq. (7)) at different timesteps.

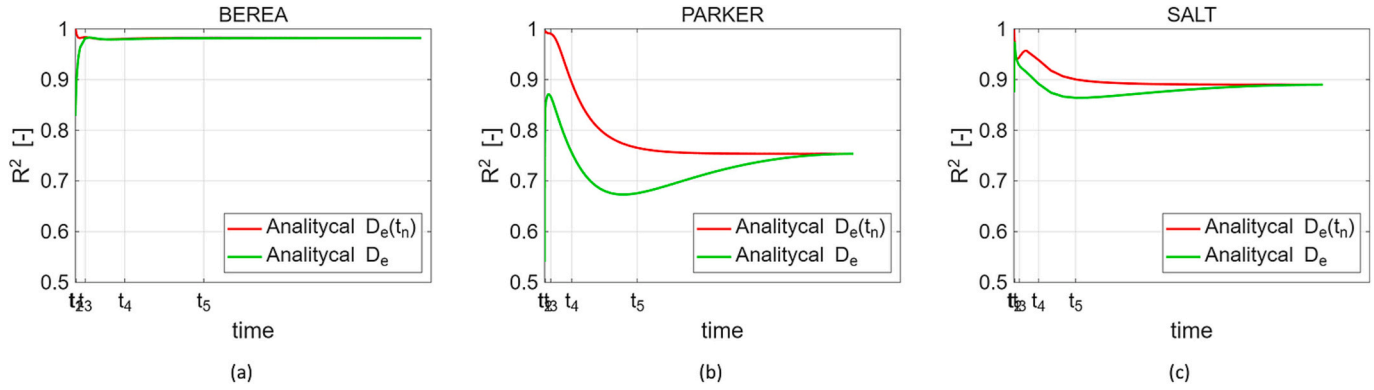

Fig. 9. Fitting error analysis for the estimate of the effective diffusivity at different simulation times.

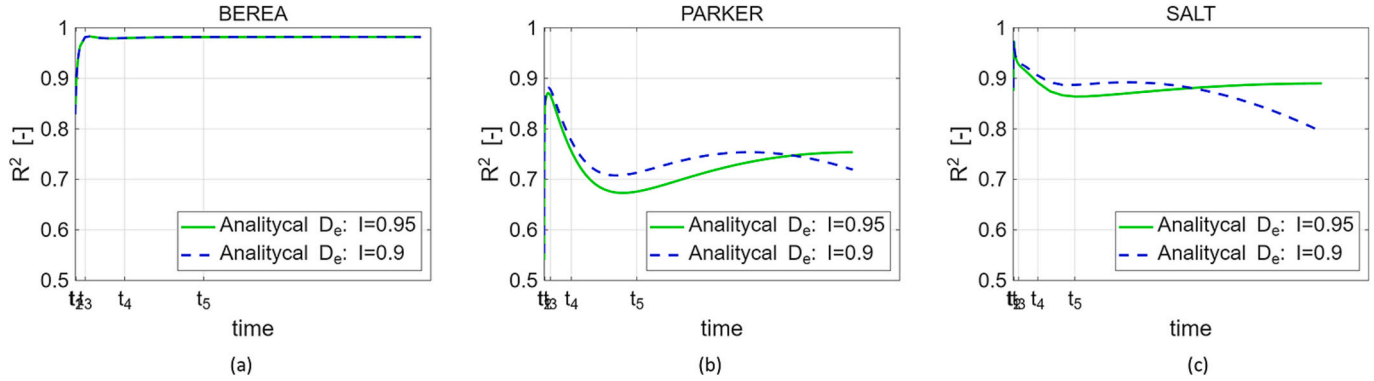

Fig. 10. Comparison of fitting error for the estimate of the effective diffusivity at different simulation times with D_e corresponding to $I(t_n) = 0.9$ (dotted blue) and $I(t_n) = 0.95$ (green). (For interpretation of the references to color in this figure legend, the reader is referred to the web version of this article.)

Parker and 0.0818 for Salt. It is pointed out that caprocks are generally tighter than the samples analyzed. Shale cap rocks exhibit a moderate bulk porosity, in the range 0.1–14% [43]. Their pore morphology is characterized by an intricate network of micropores (<2 nm) and mesopores (2–50 nm), with poor interconnection: the pore pathways exhibit significant tortuosity, typically in the range of 2–10 [7]. According to the correlation (Eq. (9)), the caprock effective diffusion is expected to be lower than the results presented here up to 3 orders of magnitude. Application of the methodology to a nano-CT image of caprock sample is recommended for a more accurate prediction.

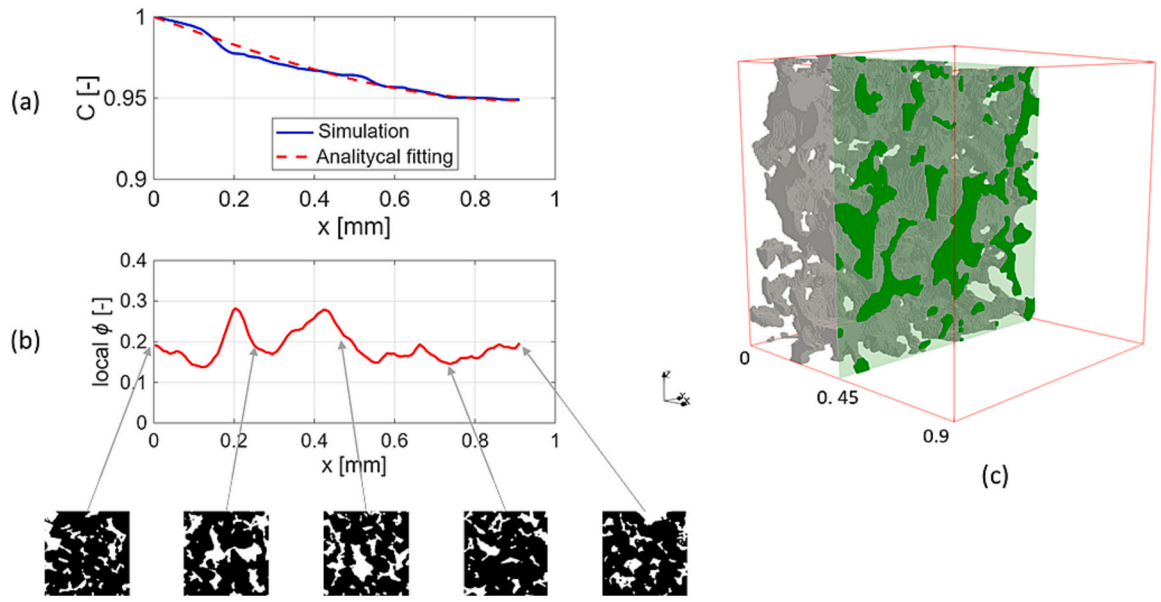

Fig. 11. Berea scenario: (a) comparison of simulated concentration profile averaged on y-z cross sections with the analytical profile obtained using the fitted diffusion coefficient in an equivalent homogeneous sample; (b) porosity calculated for y-z cross sections and example of some of the corresponding cross sections; (c) sample split to reveal the internal structure.

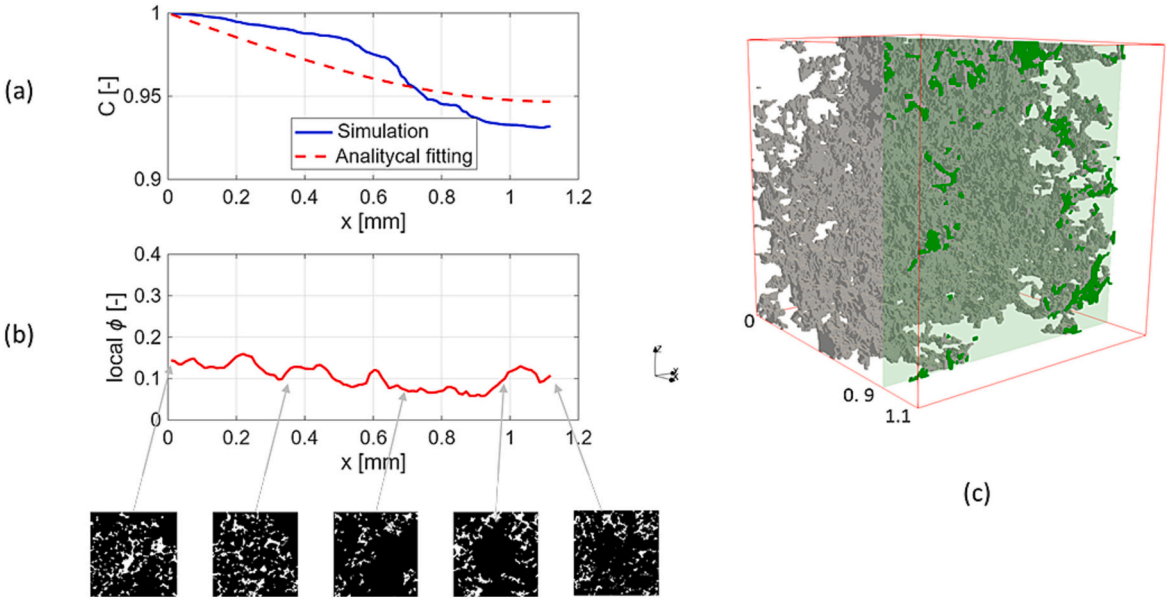

Fig. 12. Parker scenario: (a) comparison of simulated concentration profile averaged on y-z cross sections with the analytical profile obtained using the fitted diffusion coefficient in an equivalent homogeneous sample; (b) porosity calculated for y-z cross sections and example of some of the corresponding cross sections; (c) sample split to reveal the internal structure.

4. Conclusions

In the studies for the design of Underground Storage of hydrogen and carbon dioxide, the phenomenon of diffusion of gas molecules in formation water should be taken into account and properly characterized. It has an impact on various mechanisms related to the dissolution of the gases in the connate water in the reservoir zone and in the aquifers, such as the activation of microbial activity and the trapping phenomena. In the case of caprock, the diffusion coefficient defines the long-term containment of the stored or sequestered gas.

This project investigates the diffusion coefficient, with the goal of linking micro-scale processes (bulk diffusion of gas in brine at pore scale) to the macro-scale parameter (effective diffusion for continuum porous medium). The workflow relies on fitting the pore-scale numerical solution of the diffusion–transport equation to the analytical solution of Fick's second law for a homogeneous REV. Diffusion tortuosity was also estimated and compared with the geometric tortuosity, obtained using an A*- based pathfinding algorithm, and with the hydraulic tortuosity, derived from incompressible single-phase CFD simulation.

Due to the lack of nano-CT caprock data, the proposed methodology has been applied to three rock samples featuring micrometric pores and exhibiting different values of tortuosity and porosity. For the selected samples, diffusion tortuosity turned out to be higher than both hydraulic and geometric tortuosity because diffusion tends to cover all the connected pores, not only the shortest paths or the most effective paths for the flow.

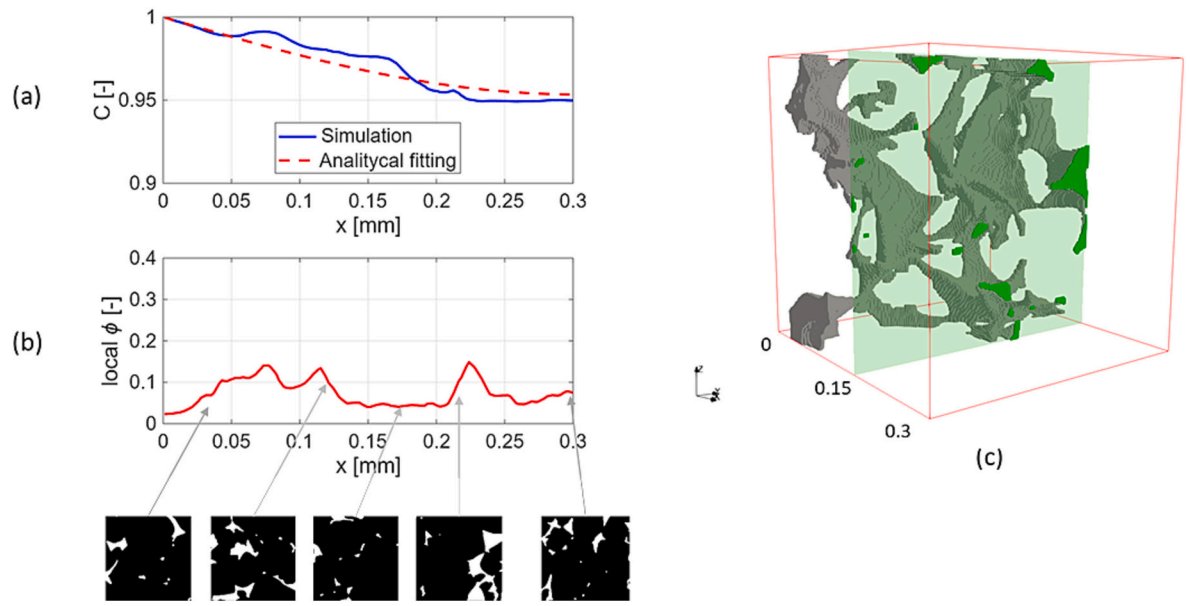

Fig. 13. Salt scenario: (a) comparison of simulated concentration profile averaged on y-z cross sections with the analytical profile obtained using the fitted diffusion coefficient in an equivalent homogeneous sample; (b) porosity calculated for y-z cross sections and example of some of the corresponding cross sections; (c) sample split in half to reveal the internal structure.

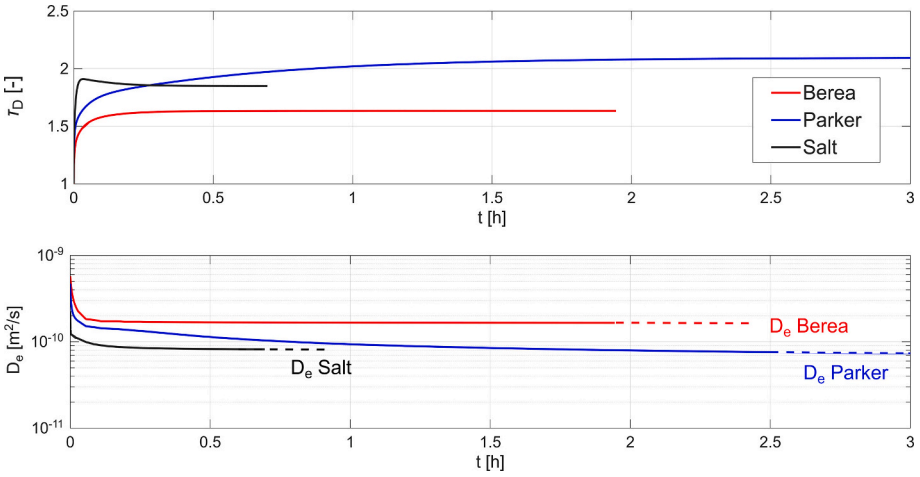

Fig. 14. Asymptotic convergence of numerical estimate of tortuosity (top) and effective diffusivity (bottom) as the domain is completely explored by diffusion phenomena.

Table 6
Tortuosity and diffusivity results.

Sample	τ_g (−)	τ_h (−)	τ_D (−)	D_e (m^2/s)	
				Correlation	Fick's law fitting
Berea	1.41	1.52	1.63	$7.53\ 10^{-11}$	$1.66\ 10^{-10}$
Parker	1.64	1.92	2.1	$2.72\ 10^{-11}$	$7.37\ 10^{-11}$
Salt	1.59	1.74	1.85	$2.34\ 10^{-11}$	$8.18\ 10^{-11}$

The effective diffusion coefficients obtained with the proposed workflow were consistent with those derived from the correlation, while still yielding a more conservative estimate. Furthermore, the diffusivity values obtained were consistent with experimental data reported in the literature for saturated sealing lithotypes. Even if equivalent from the computational point of view, being independent from any empirical correlation, the proposed approach is more directly tied to the actual pore-scale morphology described by the tomographic images.

The results presented here should be regarded as conservative values, as caprocks are expected to be tighter than the samples analyzed. The methodology can nevertheless be readily reapplied to nano-CT images of actual caprocks to obtain more accurate predictions. This would entail a non-negligible increase in computational cost, due to the image resolution being approximately 20–50 times higher. However, fine-grained caprock lithologies often possess a certain degree of spatial homogeneity at the scale of hundreds of micrometers [66], which allows reducing the representative elementary volume by approximately one order of magnitude; furthermore, low-porosity samples naturally involve fewer cells within the pore space, which constitutes the simulation domain. Other difficulties in dealing with nano-CT images regard the image binarization, which is complicated by a low signal-to-noise ratio [67]. A thorough analysis of image processing pitfalls is out of the scope of the paper.

Given the complexity and high cost of experimentally determining effective diffusion coefficients, the methodology presented here provides a means to leverage existing data to improve reservoir characterization for Underground Fluid Storage applications. On the other

hand, its applicability is constrained by the availability of high-resolution tomographic images, and its robustness is conditioned to an accurate image binarization.

The analysis could be extended in three dimensions to identify anisotropies in the sample. An additional interesting development would be to apply the methodology to domains constructed from nano-CT scans of caprock, to assess the sensitivity of the method to higher resolution and reduced diffusivity.

CRediT authorship contribution statement

Cristina Serazio: Writing – review & editing, Writing – original draft, Visualization, Validation, Software, Methodology. **Eloisa Salina Borello:** Writing – review & editing, Writing – original draft, Methodology, Data curation. **Dario Viberti:** Writing – review & editing, Supervision, Methodology, Conceptualization.

Declaration of competing interest

The authors declare that they have no known competing financial interests or personal relationships that could have appeared to influence the work reported in this paper.

Appendix A

The evolution in time and space of the solute concentration $C(x,t)$ in a finite 1D domain $[0,L]$ with not homogeneous Dirichlet condition at the inlet ($x=0$) and homogenous Neumann at the outlet ($x=L$), is described by the solution of the following differential problem

$$\begin{aligned}
&\frac{\partial C}{\partial t} = D_e \frac{\partial^2 C}{\partial x^2} \quad \forall t>0 \quad \forall x \in (0,L)\\
&C(x,0) = 0 \quad \forall x \in [0,L]\\
&C(0,t) = C_0 \quad \forall t>0\\
&\left.\frac{\partial C}{\partial x}\right|_{x=L} = 0 \quad \forall t>0
\end{aligned} \tag{A1}$$

Exploiting the linearity of the differential operator we can suppose that the solution can be expressed in the form

$$C(x,t) = v(x,t) + q(x) \tag{A2}$$

It follows that the problem (A1) can be rewritten as

$$\begin{aligned}
&\frac{\partial v}{\partial t} = D_e\left(\frac{\partial^2 v}{\partial x^2} + q''\right) \quad \forall t>0 \quad \forall x \in (0,L)\\
&v(x,0) = -q(x) \quad \forall x \in (0,L)\\
&v(0,t) = C_0 - q(0) \quad \forall t>0\\
&\left.\frac{\partial v}{xt}\right|_{x=L} = -q'(L) \quad \forall t>0
\end{aligned} \tag{A3}$$

where q' and q'' are the first and second order derivative of $q(x)$, respectively.

If the unknown term $q(x)$ satisfies the ordinary boundary value problem with Robin conditions

$$\begin{aligned}
&D_e q'' = 0 \quad \forall x \in (0,L)\\
&q(0) = C_0\\
&q'(L) = 0
\end{aligned} \tag{A4}$$

the solution $q(x) = C_0$ is trivial, and the problem (A3) results

$$\begin{aligned}
&\frac{\partial v}{\partial t} = D_e \frac{\partial^2 v}{\partial x^2} \quad \forall t>0 \quad \forall x \in (0,L)\\
&v(x,0) = -C_0 \quad \forall x \in (0,L)\\
&v(0,t) = 0 \quad \forall t>0\\
&\left.\frac{\partial v}{xt}\right|_{x=L} = 0 \quad \forall t>0
\end{aligned} \tag{A5}$$

To apply the separation of variables method to the problem (A5), it is supposed that

$$v(x,t) = X(x)T(t) \tag{A6}$$

where $X(x)$ and $T(t)$ are non trivial, i.e. $X(x) = 0 \forall x \in (0,L)$ and $T(t) = 0 \ \forall t>0$ are not acceptable solutions. Substituting Eq. (A6) in Eq. (A5) we obtain

$$\begin{aligned}
&XT' = D_e X'' T \quad \forall t>0 \quad \forall x \in (0,L)\\
&X(x)T(0) = -C_0 \quad \forall x \in (0,L)\\
&X(0)T(t) = 0 \quad \forall t>0\\
&X'(L)T(t) = 0 \quad \forall t>0
\end{aligned} \tag{A7}$$

which means that must be satisfied the condition $\forall x \in (0, L)$ and $\forall t > 0$

$$\frac{T'}{D_e T} = \frac{X''}{X} = -\lambda^2 \tag{A8}$$

where λ is an unknow constant. Now it is possible to solve the two ordinary differential equations in space and in time, separately.

The ODE in time has general solution

$$T(t) = ce^{-\lambda^2 D_e t} \tag{A9}$$

The BVP in space, instead, reduces to a regular Sturm-Liouville Problem of the form

$$\begin{aligned} &X'' + \lambda^2 X = 0 \quad \forall x \in (0, L) \\ &X(0) = 0 \\ &X'(L) = 0 \end{aligned} \tag{A10}$$

The Sturm-Liouville theory [68] proves that the solution of the problem of type (A10) is given by a series of eigenvalues, simple and real, with expression:

$$\lambda_n = \frac{(2n-1)\pi}{2L} \quad \forall n > 0 \tag{A11}$$

and the associated eigenfunctions, which represents and orthonormal basis respect to the Hilbert space $L^2(0, L)$, have expression

$$\varphi_n = \sqrt{\frac{2}{L}} \sin(\lambda_n x) \ \ \forall n > 0 \tag{A12}$$

Each function $f \in L^2(0, L)$, thus can be expressed as a Fourier's series

$$f(x) = \sum_{n=1}^{+\infty} \alpha_n \varphi_n(x) \tag{A13}$$

where

$$\alpha_n = \int_0^L f(x)\varphi_n(x)dx \tag{A14}$$

It follows that solution of the Eq. (A5) problem can be expressed as

$$v(x,t) = \sum_{i=1}^{+\infty} X_n(x)T_n(t) = \sum_{i=1}^{+\infty} \alpha_n \varphi_n(x) e^{-\lambda_n^2 D_e t} \tag{A15}$$

In particular, if the initial condition is satisfied, it holds

$$v(x,0) = \sum_{i=1}^{+\infty} X_n(x)T_n(0) = \sum_{i=1}^{+\infty} \alpha_n \varphi_n(x) = -C_0 \tag{A16}$$

where

$$\alpha_n = -C_0 \int_0^L \varphi_n(x)dx = -\sqrt{\frac{2}{L}} \frac{C_0}{\lambda_n} \tag{A17}$$

Substituting the Eq. (A17) in Eq. (A15) and, in turn, in Eq. (A2), it follows:

$$C(x,t) = C_0 \left[1 - \frac{2}{L} \sum_{i=1}^{+\infty} \frac{\sin(\lambda_n x)}{\lambda_n} e^{-\lambda_n^2 D_e t} \right] \tag{A18}$$

Data availability

Data will be made available on request.

References

[1] C. Benetatos, F. Verga, S. Bocchini, A. Carpignano, A. Chiodoni, M. Cocuzza, How Underground Systems Can Contribute to Meet the Challenges of Energy Transition. GEAM-2021-163-164-163-164 1224, 2021, pp. 65–80, https://doi.org/10.19199/2021.163-164.1121-9041.065.

[2] J. Song, D. Zhang, Comprehensive review of caprock-sealing mechanisms for geologic carbon sequestration, Environ. Sci. Technol. 47 (2013) 9–22, https://doi.org/10.1021/es301610p.

[3] IEA, CCUS in Clean Energy Transitions, Energy Technology Perspectives, Paris, https://www.iea.org/reports/ccus-in-clean-energy-transitions, 2020.

[4] D. Zivar, S. Kumar, J. Foroozesh, Underground hydrogen storage: a comprehensive review, Int. J. Hydrog. Energy 46 (2021) 23436–23462, https://doi.org/10.1016/j.ijhydene.2020.08.138.

[5] U. Bünger, H. Landinger, E. Pschorr-Schoberer, P. Schmidt, W. Weindorf, J. Jöhrens, U. Lambrecht, K. Naumann, A. Lischke, Power to gas in transport-status quo and perspectives for development, Federal Ministry of Transport and Digital Infrastructure (BMVI), Germany, 2021.

[6] M. Fleury, P. Berne, P. Bachaud, Diffusion of dissolved CO_2 in caprock, Energy Procedia 1 (2009) 3461–3468, https://doi.org/10.1016/j.egypro.2009.02.137.

[7] N.R. Backeberg, F. Iacoviello, M. Rittner, T.M. Mitchell, A.P. Jones, R. Day, J. Wheeler, P.R. Shearing, P. Vermeesch, A. Striolo, Quantifying the anisotropy and tortuosity of permeable pathways in clay-rich mudstones using models based on X-

ray tomography, Sci. Rep. 7 (2017) 14838, https://doi.org/10.1038/s41598-017-14810-1.
[8] S. Alafnan, Factors influencing hydrogen migration in cap rocks: establishing new screening criteria for the selection of underground hydrogen storage locations, Int. J. Hydrog. Energy 83 (2024) 1099–1106, https://doi.org/10.1016/j.ijhydene.2024.08.179.
[9] M. Al-Shafi, O. Massarweh, A.S. Abushaikha, Y. Bicer, A review on underground gas storage systems: natural gas, hydrogen and carbon sequestration, Energy Rep. 9 (2023) 6251–6266, https://doi.org/10.1016/j.egyr.2023.05.236.
[10] C. Benetatos, F. Catania, G. Giglio, C.F. Pirri, A. Raeli, L. Scaltrito, C. Serazio, F. Verga, Workflow for the validation of geomechanical simulations through seabed monitoring for offshore underground activities, JMSE 11 (2023) 1387, https://doi.org/10.3390/jmse11071387.
[11] C. Hemme, W. Van Berk, Hydrogeochemical modeling to identify potential risks of underground hydrogen storage in depleted gas fields, Appl. Sci. 8 (2018) 2282, https://doi.org/10.3390/app8112282.
[12] A. Vinsot, C.A.J. Appelo, M. Lundy, S. Wechner, Y. Lettry, C. Lerouge, A. M. Fernández, M. Labat, C. Tournassat, P. De Canniere, B. Schwyn, J. Mckelvie, S. Dewonck, P. Bossart, J. Delay, In situ diffusion test of hydrogen gas in the Opalinus Clay, SP 400 (2014) 563–578, https://doi.org/10.1144/SP400.12.
[13] Engineering ToolBox, Solubility of Gases in Water, 2008.
[14] W. Ou, L. Geng, W. Lu, H. Guo, K. Qu, P. Mao, Quantitative Raman spectroscopic investigation of geo-fluids high-pressure phase equilibria: part II. Accurate determination of CH4 solubility in water from 273 to 603 K and from 5 to 140 MPa and refining the parameters of the thermodynamic model, Fluid Phase Equilib. 391 (2015) 18–30, https://doi.org/10.1016/j.fluid.2015.01.025.
[15] A. Tamimi, E.B. Rinker, O.C. Sandall, Diffusion coefficients for hydrogen sulfide, carbon dioxide, and nitrous oxide in water over the temperature range 293–368 K, J. Chem. Eng. Data 39 (1994) 330–332, https://doi.org/10.1021/je00014a031.
[16] M. Tawil, E. Salina Borello, S. Bocchini, C.F. Pirri, F. Verga, C. Coti, M. Scapolo, D. Barbieri, D. Viberti, Solubility of H2-CH4 mixtures in brine at underground hydrogen storage thermodynamic conditions, Front. Energy Res. 12 (2024) 1356491, https://doi.org/10.3389/fenrg.2024.1356491.
[17] R. Weibe, V.L. Gaddy, J.C. Heins, Solubility of hydrogen in water at 25 °C from 25 to 1000 atmospheres, Ind. Eng. Chem. 24 (1932) 823–825, https://doi.org/10.1021/ie50271a024.
[18] D.L. Wise, G. Houghton, The diffusion coefficients of ten slightly soluble gases in water at 10–60°C, Chem. Eng. Sci. 21 (1966) 999–1010, https://doi.org/10.1016/0009-2509(66)85096-0.
[19] J. Van Brakel, P.M. Heertjes, Analysis of diffusion in macroporous media in terms of a porosity, a tortuosity and a constrictivity factor, Int. J. Heat Mass Transf. 17 (1974) 1093–1103, https://doi.org/10.1016/0017-9310(74)90190-2.
[20] R.H. Perry, D.W. Green (Eds.), Perry's Chemical Engineers' Handbook, 8 ed., McGraw-Hill, New York, NY, 2008.
[21] C.R. Wilke, P. Chang, Correlation of diffusion coefficients in dilute solutions, AIChE J. 1 (1955) 264–270, https://doi.org/10.1002/aic.690010222.
[22] M. Aertsens, Re-evaluation of the experimental data of the MEGAS experiment on GasMigration through boom-clay. (No. SCK CEN-ER-100.), SCK CEN, Mol, Belgium, 2009.
[23] F. Bardelli, C. Mondelli, M. Didier, J.G. Vitillo, D.R. Cavicchia, J.-C. Robinet, L. Leone, L. Charlet, Hydrogen uptake and diffusion in Callovo-Oxfordian clay rock for nuclear waste disposal technology, Appl. Geochem. 49 (2014) 168–177, https://doi.org/10.1016/j.apgeochem.2014.06.019.
[24] M. Didier, L. Leone, J.-M. Greneche, E. Giffaut, L. Charlet, Adsorption of hydrogen gas and redox processes in clays, Environ. Sci. Technol. 46 (2012) 3574–3579, https://doi.org/10.1021/es204583h.
[25] E. Jacops, K. Wouters, G. Volckaert, H. Moors, N. Maes, C. Bruggeman, R. Swennen, R. Littke, Measuring the effective diffusion coefficient of dissolved hydrogen in saturated Boom Clay, Appl. Geochem. 61 (2015) 175–184, https://doi.org/10.1016/j.apgeochem.2015.05.022.
[26] B.M. Krooss, Evaluation of Database on Gas Migration Through Clayey Host Rocks, Belgian National Agency for Radioactive Waste and Enriched Fissile Material (ONDRAF-NIRAS), Aachen, Germany, 2008.
[27] J. Michelsen, B. Hagemann, L. Ganzer, W. Hujer, Measurement of hydrogen diffusion through caprock samples, in: Sixth International Conference on Fault and Top Seals, Presented at the Sixth International Conference on Fault and Top Seals, European Association of Geoscientists & Engineers, Vienna, Austria, 2022, pp. 1–5, https://doi.org/10.3997/2214-4609.202243061.
[28] E. Salina Borello, S. Bocchini, A. Chiodoni, C. Coti, M. Fontana, F. Panini, C. Peter, C.F. Pirri, M. Tawil, A. Mantegazzi, F. Marzano, V. Pozzovivo, F. Verga, D. Viberti, Underground hydrogen storage safety: experimental study of hydrogen diffusion through caprocks, Energies 17 (2024) 394, https://doi.org/10.3390/en17020394.
[29] G. Volckaert, L. Ortiz, P. De Cannière, M. Put, S.T. Horseman, J.F. Harrington, V. Fioravante, M. Impey, MEGAS Modelling and Experiments on Gas Migration in Repository Host Rocks. (No. EUR16235 EN.), 1994 (Luxembourg).
[30] A. Busch, S. Alles, Y. Gensterblum, D. Prinz, D.N. Dewhurst, M.D. Raven, H. Stanjek, B.M. Krooss, Carbon dioxide storage potential of shales, Int. J. Greenh. Gas Con. 2 (2008) 297–308, https://doi.org/10.1016/j.ijggc.2008.03.003.
[31] A. Hildenbrand, B.M. Krooss, CO_2 migration processes in argillaceous rocks: pressure-driven volume flow and diffusion, J. Geochem. Explor. 78–79 (2003) 169–172, https://doi.org/10.1016/S0375-6742(03)00077-3.
[32] B. Krooss, A. Hildenbrand, S. Alles, R. Littke, J. Pearce, Assessment of the CO_2 sealing efficiency of pelitic rocksTwo-phase flow and diffusive transport, in: Greenhouse Gas Control Technologies 7, Elsevier, 2005, pp. 2003–2006, https://doi.org/10.1016/B978-008044704-9/50259-7.
[33] J. Wollenweber, S. Alles, A. Busch, B.M. Krooss, H. Stanjek, R. Littke, Experimental investigation of the CO_2 sealing efficiency of caprocks, Int. J. Greenh. Gas Con. 4 (2010) 231–241, https://doi.org/10.1016/j.ijggc.2010.01.003.
[34] J. Wollenweber, S.A. Alles, A. Kronimus, A. Busch, H. Stanjek, B.M. Krooss, Caprock and overburden processes in geological CO_2 storage: an experimental study on sealing efficiency and mineral alterations, Energy Procedia 1 (2009) 3469–3476, https://doi.org/10.1016/j.egypro.2009.02.138.
[35] C. Greenshields, OpenFOAM v11 User Guide, The OpenFOAM Foundation, London, UK, 2023.
[36] T.W. Ridler, S. Calvard, Picture thresholding using an iterative selection method, IEEE Trans. Syst. Man Cybern. Syst. 8 (1978) 630–632, https://doi.org/10.1109/TSMC.1978.4310039.
[37] M. Kampschulte, A. Langheinirch, J. Sender, H. Litzlbauer, U. Althöhn, J. Schwab, E. Alejandre-Lafont, G. Martels, G. Krombach, Nano-computed tomography: technique and applications, Fortschr. Röntgenstr. 188 (2016) 146–154, https://doi.org/10.1055/s-0041-106541.
[38] H. Dong, M.J. Blunt, Pore-network extraction from micro-computerized-tomography images, Phys. Rev. E 80 (2009) 036307, https://doi.org/10.1103/PhysRevE.80.036307.
[39] Imperial College Consortium On Pore-Scale Imaging and Modelling, Berea Sandstone, 2014, https://doi.org/10.6084/M9.FIGSHARE.1153794.V2.
[40] S. Ghanbarzadeh, M.A. Hesse, M. Prodanovic, J.E. Gardner, Synthetic Rock Salt, 2015, https://doi.org/10.17612/P7MW21.
[41] R. Neumann, M. Andreeta, E. Lucas-Oliveira, 11 Sandstones: Raw, Filtered and Segmented Data, 2020, https://doi.org/10.17612/F4H1-W124.
[42] R.F. Neumann, M. Barsi-Andreeta, E. Lucas-Oliveira, H. Barbalho, W.A. Trevizan, T.J. Bonagamba, M.B. Steiner, High accuracy capillary network representation in digital rock reveals permeability scaling functions, Sci. Rep. 11 (2021), https://doi.org/10.1038/s41598-021-90090-0.
[43] P.-M. Trimi, S. Bellas, I. Vakalas, R. Gholami, V. Gaganis, E. Gontikaki, E. Stamatakis, I. Yentekakis, A review of caprock integrity in underground hydrogen storage sites: implication of wettability, interfacial tension, and diffusion, Hydrogen 6 (2025) 91, https://doi.org/10.3390/hydrogen6040091.
[44] M. Fleury, S. Gautier, N. Gland, P.F. Boulin, B. Norden, C. Schmidt-Hattenberger, Advanced and integrated petrophysical characterization for CO_2 storage: application to the Ketzin site, Oil Gas Sci. Technol. 68 (2013) 557–576, https://doi.org/10.2516/ogst/2012084.
[45] Y. Liu, Y. Yao, D. Liu, S. Zheng, G. Sun, Y. Chang, Shale pore size classification: an NMR fluid typing method, Mar. Pet. Geol. 96 (2018) 591–601, https://doi.org/10.1016/j.marpetgeo.2018.05.014.
[46] C. Ma, C. Lin, C. Dong, D. Elsworth, S. Wu, X. Wang, X. Sun, Determination of the critical flow pore diameter of shale caprock, Mar. Pet. Geol. 112 (2020) 104042, https://doi.org/10.1016/j.marpetgeo.2019.104042.
[47] A. Paul, T. Laurila, V. Vuorinen, S.V. Divinski, Fick's laws of diffusion, in: Thermodynamics, Diffusion and the Kirkendall Effect in Solids, Springer International Publishing, Cham, 2014, pp. 115–139, https://doi.org/10.1007/978-3-319-07461-0_3.
[48] N. Epstein, On tortuosity and the tortuosity factor in flow and diffusion through porous media, Chem. Eng. Sci. 44 (1989) 777–779, https://doi.org/10.1016/0009-2509(89)85053-5.
[49] J. Fu, H.R. Thomas, C. Li, Tortuosity of porous media: image analysis and physical simulation, Earth Sci. Rev. 212 (2021) 103439, https://doi.org/10.1016/j.earscirev.2020.103439.
[50] P.G. Haddad, M. Ranchou-Peyruse, M. Guignard, J. Mura, F. Casteran, L. Ronjon-Magand, P. Senechal, M.-P. Isaure, P. Moonen, G. Hoareau, D. Dequidt, P. Chiquet, G. Caumette, P. Cezac, A. Ranchou-Peyruse, Geological storage of hydrogen in deep aquifers – an experimental multidisciplinary study, Energy Environ. Sci. 15 (2022) 3400–3415, https://doi.org/10.1039/D2EE00765G.
[51] B. Tjaden, J. Lane, P.J. Withers, R.S. Bradley, D.J.L. Brett, P.R. Shearing, The application of 3D imaging techniques, simulation and diffusion experiments to explore transport properties in porous oxygen transport membrane support materials, Solid State Ionics 288 (2016) 315–321, https://doi.org/10.1016/j.ssi.2016.01.030.
[52] A. Wheeler, Catalysis II, Reinhold, New York, 1955.
[53] J.A. Currie, Gaseous diffusion in porous media part 1. - a non-steady state method, Br. J. Appl. Phys. 11 (1960) 314–317, https://doi.org/10.1088/0508-3443/11/8/302.
[54] E.L. Cussler, Diffusion: Mass Transfer in Fluid Systems, Univ. Press, Cambridge, 1984.
[55] P. Grathwohl, Diffusion in natural porous media: contaminant transport, sorption/desorption and dissolution kinetics, in: Topics in Environmental Fluid Mechanics, Springer US, Boston, MA, 1998, https://doi.org/10.1007/978-1-4615-5683-1.
[56] E. Salina Borello, C. Peter, F. Panini, D. Viberti, Application of A* algorithm for microstructure and transport properties characterization from 3D rock images, Energy 239 (2022) 122151, https://doi.org/10.1016/j.energy.2021.122151.
[57] A.F. Ismail, Gas Separation Membranes: Polymeric and Inorganic, Springer International Publishing AG, Cham, 2015.
[58] B. Ghanbarian, A.G. Hunt, R.P. Ewing, M. Sahimi, Tortuosity in porous media: a critical review, Soil Sci. Soc. Am. J. 77 (2013) 1461–1477, https://doi.org/10.2136/sssaj2012.0435.
[59] F. Panini, B. Ghanbarian, E. Salina Borello, D. Viberti, Estimating geometric tortuosity of saturated rocks from micro-CT images using percolation theory, Transp. Porous Media (2024), https://doi.org/10.1007/s11242-024-02085-w.
[60] F. Panini, E. Salina Borello, C. Peter, D. Viberti, Application of a* algorithm for tortuosity and effective porosity estimation of 2D rock images, in: D.A. Indeitsev, A.M. Krivtsov (Eds.), Advanced Problem in Mechanics II, Lecture Notes in

Mechanical Engineering, Springer International Publishing, Cham, 2022, pp. 519–530, https://doi.org/10.1007/978-3-030-92144-6_39.
[61] A. Raeli, E. Salina Borello, F. Panini, C. Serazio, D. Viberti, A parallel programming application of the A* algorithm in digital rock physics, Comput. Geosci. (2024) 105578, https://doi.org/10.1016/j.cageo.2024.105578.
[62] D. Viberti, C. Peter, E. Salina Borello, F. Panini, Pore structure characterization through path-finding and Lattice Boltzmann simulation, Adv. Water Resour. 141 (2020) 103609, https://doi.org/10.1016/j.advwatres.2020.103609.
[63] Y. Zhang, Z. Yang, F. Wang, X. Zhang, Comparison of soil tortuosity calculated by different methods, Geoderma 402 (2021) 115358, https://doi.org/10.1016/j.geoderma.2021.115358.
[64] M.B. Clennell, Tortuosity: A Guide Through the Maze. SP 122, 1997, pp. 299–344, https://doi.org/10.1144/GSL.SP.1997.122.01.18.
[65] R. Allen, S. Sun, Computing and comparing effective properties for flow and transport in computer-generated porous media, Geofluids 2017 (2017) 1–24, https://doi.org/10.1155/2017/4517259.
[66] L.M. Keller, L. Holzer, P. Schuetz, P. Gasser, Pore space relevant for gas permeability in Opalinus clay: statistical analysis of homogeneity, percolation, and representative volume element, JGR Solid Earth 118 (2013) 2799–2812, https://doi.org/10.1002/jgrb.50228.
[67] W. Tang, M. Li, Scalable double regularization for 3D Nano-CT reconstruction, J. Pet. Sci. Eng. 192 (2020) 107271, https://doi.org/10.1016/j.petrol.2020.107271.
[68] W.E. Boyce, R.C. DiPrima, C.W. Haines, Elementary Differential Equations and Boundary Value Problems, Wiley, New York, 1969.